Stall behavior of a two-element high-lift airfoil in disturbed flow

David Hahn*, Peter Scholz† and Rolf Radespiel‡
Institute of Fluid Mechanics, Technische Universität Braunschweig,
38108 Braunschweig, Germany

Abstract

In this publication experimental investigations treating the effects of large scale disturbances on an airfoil are reported. As disturbances quasi two-dimensional transversal vortices are created in a closed test-section shortly after the nozzle. Convecting along the test section, these vortices interact with a two-element airfoil in high lift configuration further downstream. To identify and characterize these interactions, several measurement techniques, like Particle Image Velocimetry (PIV), time resolved static pressure measurements, measurements of the static pressure distribution of the high-lift airfoil, oil flow visualization and Five Hole Probe (FHP) measurements are utilized.

1 Introduction

Aircraft move within an atmospheric, turbulent boundary layer. Especially during high-lift periods, e.g. landing and take off, disturbances in that layer might have a strong impact on aircraft behavior. As atmospheric disturbances are predominantly three dimensional and have a high range of frequencies, their interactions with aircraft lift is very difficult to predict. In order to design future high-lift systems towards these critical periods of flight, it is obligatory to understand the interactions between atmospheric phenomena and the flow around the airfoil, respectively around the aircraft. To date, neither the computational simulation of a realistic flight of an airplane through a real atmosphere, nor the experimental simulation of generic atmospheric disturbances in a wind tunnel test-section have been realized in a reproducible way.

The DFG sponsored research project "Simulation of the Stall Behavior of Wings and Engine Nacelles", FOR 1066, is examining the interactions of atmospheric disturbances with a wing and an engine nacelle in both ways, theoretically by CFD calculations and experimentally by wind tunnel studies. As a part of this research project, the Technische Universität Braunschweig performs experimental investigations to establish a high quality database [4] of the stall

*Research Engineer.
†Head of Group "Flow Control and Measuring Techniques".
‡Professor and Head of Institute.

behavior for the DLR-F 15 high-lift airfoil [15] in disturbed flow [5]. Transversal quasi two-dimensional vortices, representing realistic atmospheric up- and down-winds [7], were identified as a reasonable starting point. Single vortices in a vertical plane can be created and investigated with manageable effort. Basically, experimenters have two possibilities to investigate objects in disturbed flow. Either the object that is under investigation is moved in a way, that the flow around it results in the required phenomena (e.g. helicopter rotor research [11]), or specific flow distortion is introduced upstream of the object (e.g. turbulence grid [14], flexible wings/flaps [10], [3]).

Creating specific flow distortions upstream of the airfoil being under investigation was the favored method to meet the requirements of high reproducibility. After evaluating pros and cons of active and passive methods of flow control, an active method was chosen as described in Chapter 2. For further information and details on the selection process of methods to produce generic atmospheric disturbances in a test setup refer to [6].

In Chapter 2, an overview of the utilized experimental setup and its principles is given. Chapter 3 describes the conducted investigations and their results. Finally, Chapter 4 gives a conclusion and an outlook on future investigations.

2 Experimental setup

Creating transversal quasi two-dimensional vortices in a closed wind tunnel test-section is a task, that asks for considerable effort. Figure 1 displays the principle of the test setup used for the present research, including a vortex generator and a high-lift airfoil. Here, only a short overview of the hardware setup and its design will be given. For a more detailed description see [6].

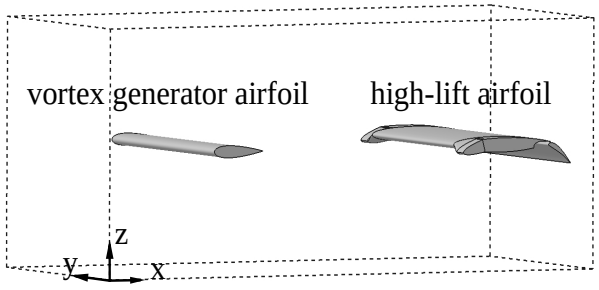

Figure 1: Assembly sketch of the vortex generator and the high-lift airfoil in the test-section.

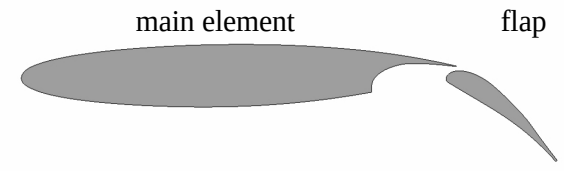

Figure 2: Contour of the two-element high-lift airfoil DLR-F 15.

A symmetric two-dimensional and in pitch direction rotatable NACA 0021 airfoil (vortex generator airfoil) with a chord length of $c_{vg} = 0.3$ m, is used to create quasi two-dimensional transversal vortices. As the vortex generator airfoil changes its angle of attack by $\Delta\alpha_{vg}$, it changes its circulation and a turbulent layer of vorticity is created in the vortex generator wake. Crucial at this is the time Δt of the pitch, which determines whether the turbulent shear layer rolls up into a start/stop-vortex or not. Δt also determines the spatial dimensions of the created disturbance. Further, the change in angle of attack $\Delta\alpha_{vg}$ defines the created vorticity [12] or the vortex circulation, respectively. To create a series of start/stop-vortices, the vortex generator needs to accelerate out of and into stagnation with a certain time of hold between each pitch. During the presented investigations a pitching velocity of approximately 0.7 °/ms and a change in angle of attack of $\Delta\alpha_{vg} = 10°$ was performed. This created start/stop-vortices

of reasonable size and vorticity. A holding time of 0.2 s between each change in angle of attack $\pm\Delta\alpha_{vg}$ completed the pitch cycles ([6]).

A DLR-F 15 contoured two-element airfoil model is integrated into a low-speed wind tunnel (MUB Modell Unterschall-Windkanal Braunschweig [6]). The airfoil with a chord length of $c_{hl} = 0.6$ m was used in high-lift configuration (FS#1 configuration [6]), see Figure 2, to investigate its interactions with the vortices created upstream. In order to investigate a relatively large model in a relatively small test-section, local sidewall droop-noses are integrated into the high-lift airfoil, as displayed in Figure 1. These local, small devices prevent sidewall boundary layer induced separations [4]. The two airfoils are installed at a distance of 2 m from each other.

For time averaged static pressure measurements 55 pressure taps in the center plane of the main element and 30 taps in the center plane of the flap were used. A PSI 8400 SDI multichannel pressure scanner with a 0.05 % full scale output accuracy was used to acquire the data. All presented lift curves are uncorrected integrals of the static pressure measurements, which means $c_{N,P}$ over α_{hl} [1]. No wind tunnel corrections are applied. For time resolved pressure measurements a FHP equipped with Kulite XCQ 62 sensors [6] [13] was used, as well as XCQ 93 sensors in the airfoil surface. Furthermore phase locked PIV measurements have been performed. An optical trigger was mounted to one actuator of the vortex generator drive. Once adjusted, reproducibility of this trigger signal is better than the sampling rate of its control, which is 3 kHz. Depending on the size of the investigated area one or two Litron Nano T double pulse lasers with a wavelength of 532 nm were used in combination with a LaVision Imager Pro X 11M camera, a Zeiss Macro-Planar T 2/50 lens and LaVision's DaVis 7 software for acquisition and evaluation. Each time series includes 300 double pictures and after the evaluation process the spatial resolution is 2 mm (for more details see [6]). DEHS seeding was injected into the wind tunnel settling chamber as droplets of an average size of 1 μm [9]. In all presented investigations free stream velocity is adjusted to 50 m/s in the $1.3 * 1.3 * 6\ m^3$ test-section, to achieve a Reynolds number of $\mathrm{Re} = 2 * 10^6$ at the high-lift airfoil.

3 Results

In this chapter measurements of the high-lift airfoil interacting with the upstream created vortices and their interpretation will be presented. The characteristics of the vortices in an otherwise empty test-section and their detailed evolution and convection is not part of this publication, but more information on these topics can be found in [5] and [6].

3.1 Overall airfoil flow

In this research work the focus is on simulating generic atmospheric disturbances and studying their interactions with the implemented high-lift airfoil. Nevertheless, before interpreting these dynamic interactions, it is essential to discuss the high-lift airfoil characteristics in a steady environment. In Figure 3 a comparison of measured lift-curves of the DLR-F 15 two-element airfoil in FS#1 configuration in an otherwise empty test-section (Solo) and with preceding vortex generator statically deflected (Tandem) by $\alpha_{vg} = 0°$ and $\alpha_{vg} = 10°$ is shown. As can be seen, the lift behavior of the airfoil is linear up to $\alpha_{hl} = 4°$, thereafter viscous effects start to influence the lift slope. Only near stall the lift curves differ slightly. The flap-flow of the high-lift airfoil is partly detached at low angles of attack up to $\alpha_{hl} = 3°$ to 6°. Figure 4 shows oil flow visualization on the high-lift airfoil suction side at $\alpha_{hl} = 0°; 4°; 6°$ looking upstream from

trailing to leading edge. At angles of $\alpha_{hl} = 0°$ and $4°$, the flow separates from the flap, with separation areas reaching from the flap trailing edge to $\approx 50\%$ of the flap chord. The separated areas become smaller with further increased angle of attack, since the increased circulation of the main element forces the flap-flow to stay attached. Only local separation at the trailing edge were observed for $\alpha_{hl} = 6°$.

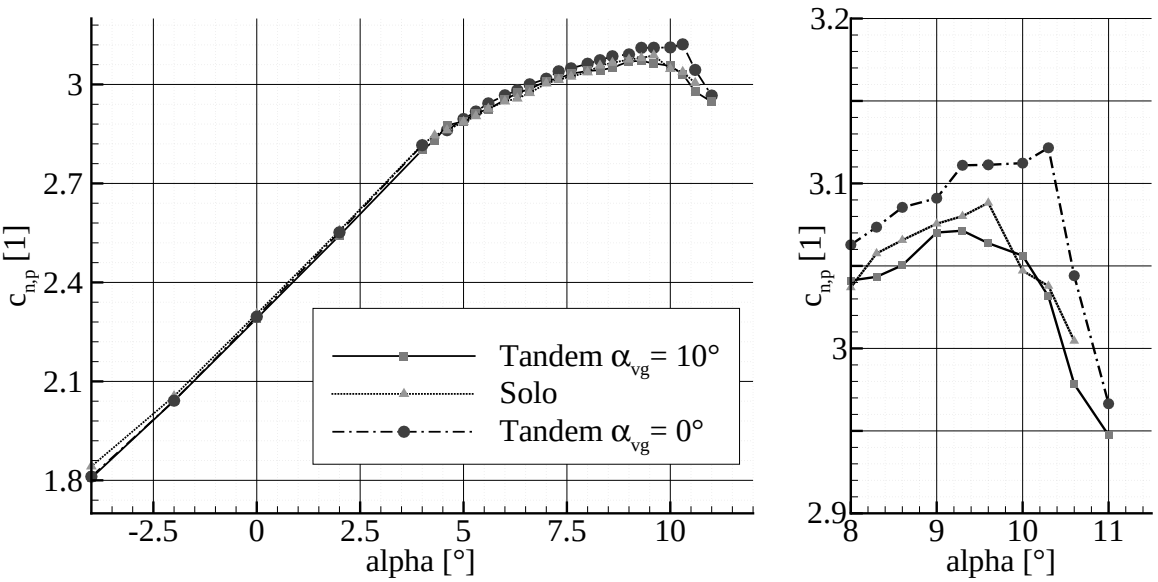

Figure 3: Comparison of DLR-F 15 lift-curves; measured without vortex generator and with statically deflected vortex generator.

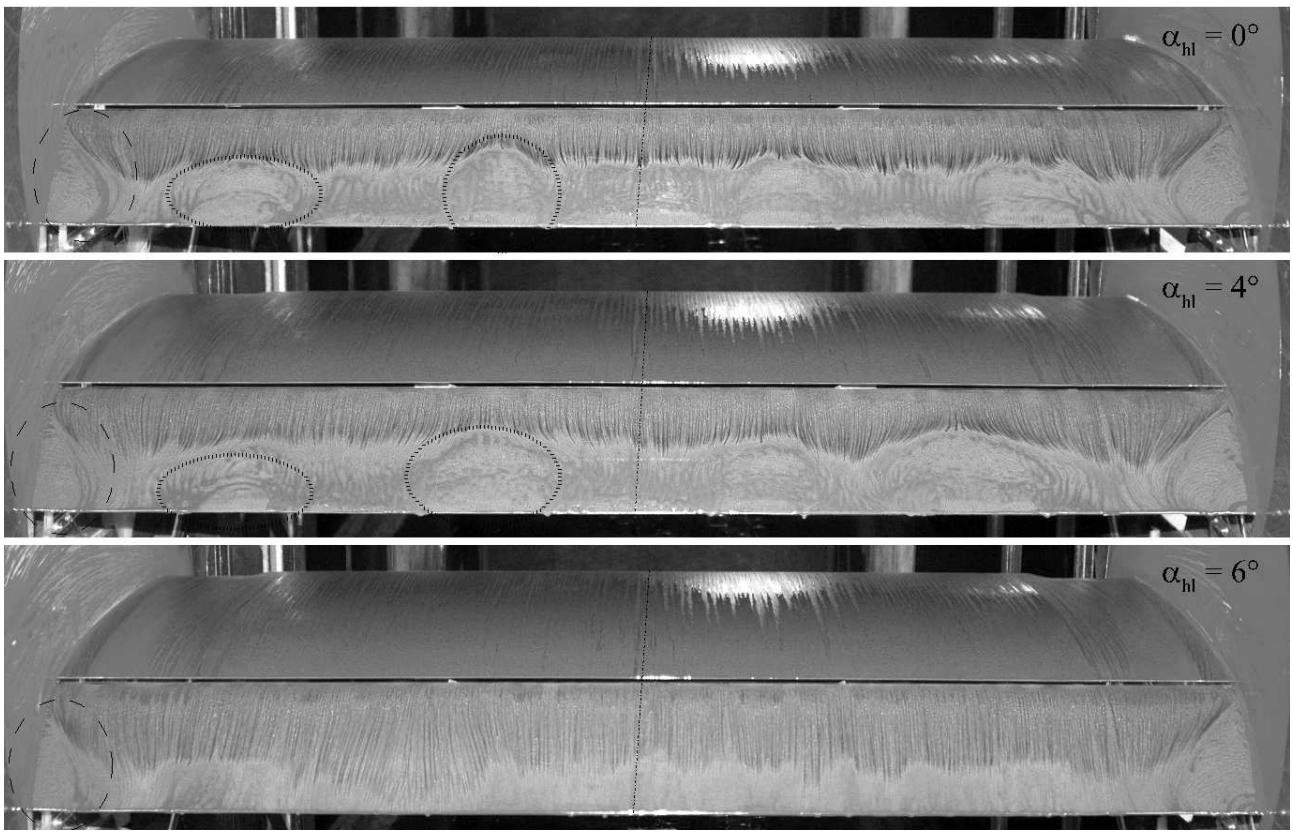

Figure 4: Oil flow visualization on the high-lift airfoil at $\alpha_{hl} = 0°; 4°; 6°$ with $\alpha_{vg} = 0°$

Figure 4 also shows the local character of the flap-separations. Local stall-cells [2] occur symmetrically to the mid-span and are surrounded on the left half-span. For all angles of attack corner separations (marked with dashed lines) appear at the intersections of the sidewall and the flap. Displacement effects of the local stall-cells interact in a way, that locally attached flap-flow can emerge. Such behavior can be seen e.g. between the corner separation and the outer separation.

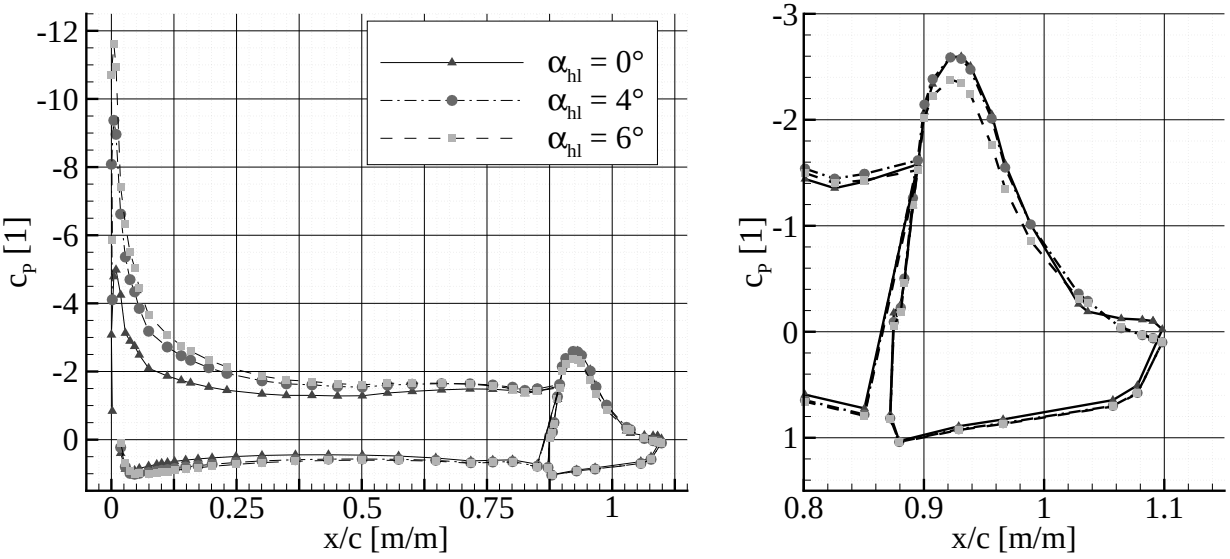

Figure 5: Static pressure distribution of DLR-F 15 measured in the MUB with $\alpha_{vg} = 0°$

Figure 5 displays the static pressure distribution on the high-lift airfoil for $\alpha_{hl} = 0°; 4°; 6°$. All pressure taps used for these measurements are located in the center section of the airfoil. Positive pressure at the flap trailing edge indicates an attached flap-flow. Figure 5 and Figure 4 show, that this is mostly the case for $\alpha_{hl} = 6°$ except for the corner separations. For an angle of attack of $\alpha_{hl} = 4°$ attached flap-flow occurs locally in the center plane area, the measurement plane.

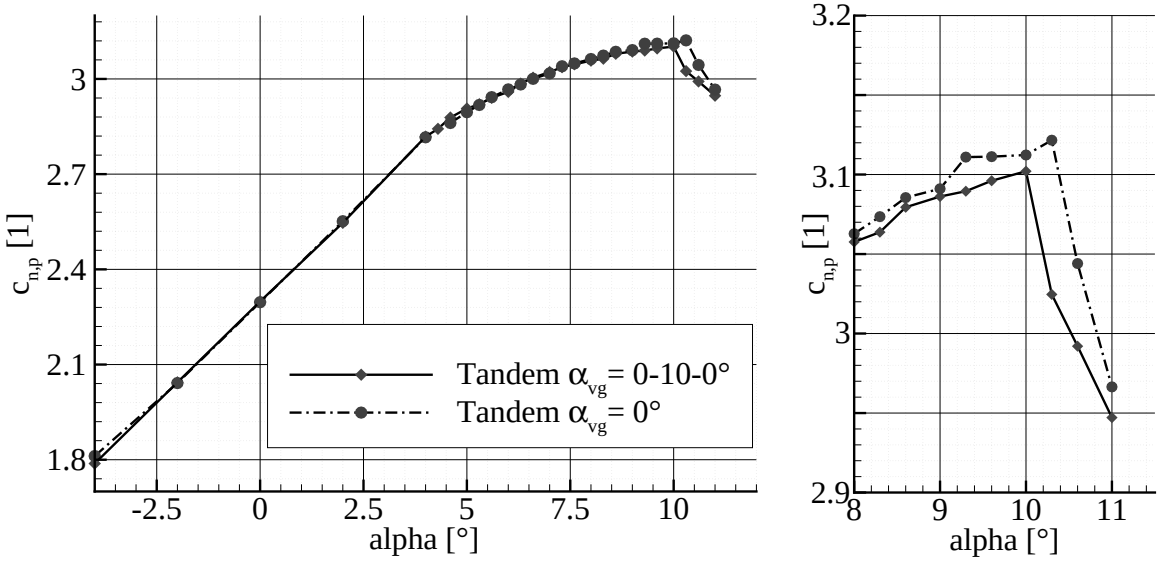

Figure 6: Comparison of lift-curves with statically undeflected vortex generator and with pitching vortex generator.

To get an impression of the overall flow of the high-lift airfoil under the influence of dynamic disturbances, Figure 6 shows a comparison of the lift curve in steady flow (undeflected vortex

generator, Tandem $\alpha_{vg} = 0°$) and in disturbed flow with a pitching vortex generator (Tandem $\alpha_{vg} = 0 - 10 - 0°$). All measurements in disturbed flow represent an average of the integration of static pressure measurements over multiple pitching cycles (> 50). Through this time integration, the time share of creating disturbances lasts only for about 10 % of the pitching cycle. Comparing the displayed lift curves, it can be concluded, that the created vortices only have a slight influence on the integral performance of the high-lift airfoil up to stall conditions. This statement is only verified for the performed pitch cycle mode (see Chapter 2).

3.2 Airfoil in disturbed flow

While Chapter 3.1 displays the overall characteristics of the high-lift airfoil, this chapter presents time-resolved measurements made in disturbed flow. All investigations were conducted at angles of attack for the high-lift airfoil far off the stall angle, as the trailing edge of the main element in combination with the flap and its gap form a complex interacting system of boundary layers, pressure gradients and gap flow. Angles of attack were selected for which dynamic disturbances can lead to a change in flap flow. For $\alpha_{hl} = 0°$ the flap flow is detached, for $\alpha_{hl} = 4°$ an increase in angle of attack leads into the non linear part of the lift-curve and for $\alpha_{hl} = 6°$ the flap flow might change between being detached and attached (compare Chapter 3.1).

3.2.1 Disturbances reaching the leading edge

By using the test setup described in Chapter 2 it is possible to create quasi two-dimensional vortices in a closed test-section as shown in [5]; [6] in more detail. The following FHP measurements are shown to give an impression of the vortices effects.

In Figure 7 over 80 cycles ensemble averaged FHP measurements (black lines) and their added / subtracted standard deviations (grey lines) are displayed. The location of the point measurements are y = 50 mm off the center section and the origin of the x-z coordinate system, referred to in the figure, is located at the nose-point of the high-lift airfoil at an angle of attack of $\alpha_{hl} = 0°$. All abscissae display time courses. All ordinates display the measured flow direction angle φ in the x-z plane (see Figure 1). Each measured φ angle consists of both, the streamline deviation (average angle shift) caused by the high-lift airfoil and the induced vortices (transient phenomena). Figure 7 a) displays the measurements of an entire ensemble averaged pitch cycle with a start- (t $\approx$ 0.04 s) and a stop-vortex (t $\approx$ 0.27 s) to illustrate the symmetry of the created start/stop-vortices. However, in Figure 7 b), c), d) only the start vortex is shown for $\alpha_{hl} = 0°, 4°, 6°$, as this vortex type is used to explain the vortex effects.

The trailing edge of the vortex generator and the leading edge of the high-lift airfoil are Δx = 2 m apart from each other and the start-vortex is induced to the flow at t = 0.00 s. It convects downstream with $u_C \simeq u_\infty = 50$ m/s, hence its flow-response in form of an induced flow-angle, passes the measurement x-position at t $\approx$ 0.04 s. By comparing the deviation of the flow-field caused by the change in angle of attack - mean value between time t = 0.1 s and t = 0.15 s in Figure 7 b),c),d) - the quasi linear relation of increasing circulation can be determined (compare lift-curve Figure 6). It is remarkable, that only the leading flank of the induced vortices (up-winds) was measured with its distinct characteristic during these measurements. However, the trailing flank of the induced vortex (down-winds) was measured only in rudiments of about $\varphi = 0.25°$.

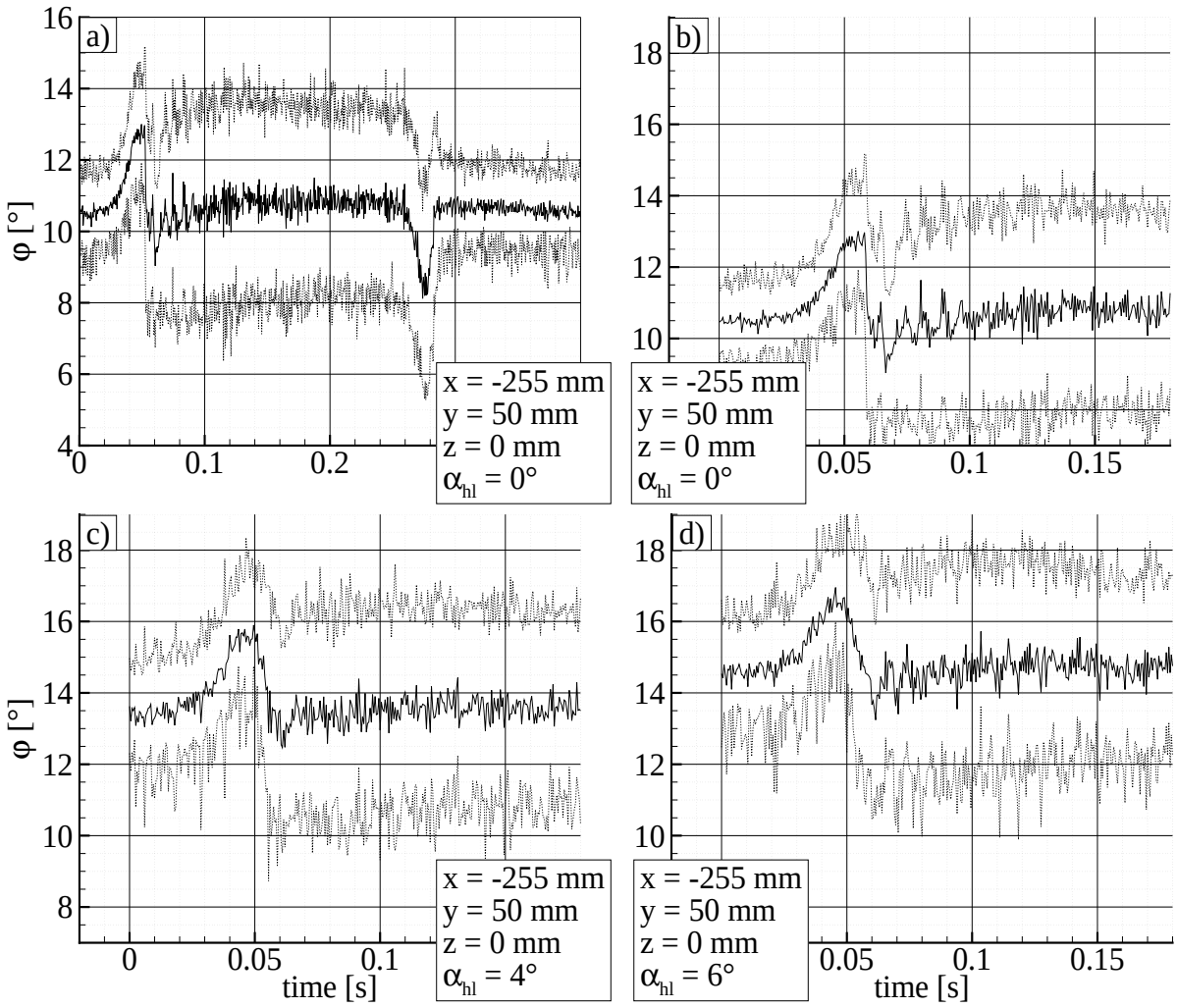

Figure 7: Ensemble averaged FHP measurements and their standard deviation ($\alpha_{hl} = 0°; 4°; 6°$)

Figure 8 shows a comparison of FHP measurements, as described above, with a vortex generator airfoil and a high-lift airfoil in the test-section (Tandem) and FHP measurements of the vortices in otherwise empty test-section (Solo). Both measurements are ensemble averaged over 80 cycles. As the x-position of the two measurements differed by $\Delta x = 355$ mm, the "Solo" measurements are shifted by 7.1 ms for comparison ($\triangleq$ 50 m/s free stream velocity). A remaining time shift of the "Solo" curve versus the "Tandem" can be explained by a slightly higher local average flow velocity with the DLR-F 15 airfoil in the test-section (Tandem, displacement effects). However, in the presence of the high-lift airfoil not only the trailing flank of the

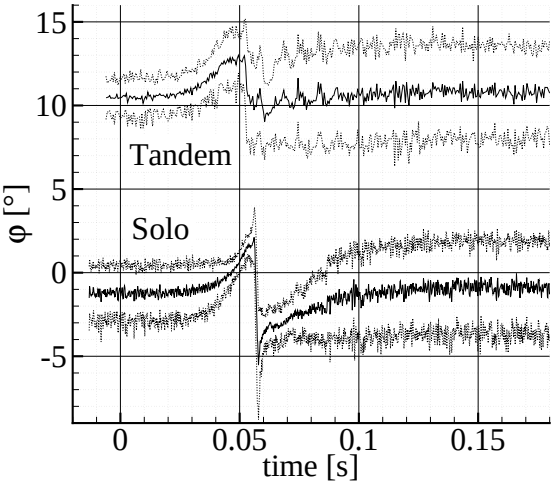

Figure 8: Comparison of the induced vortex signal with (Tandem) and without (Solo) DLR-F15 airfoil

vortices is strongly damped, but also the sharpness of the leading flank is reduced, although the maximum induced angles remain comparable.

As a next step, the two-dimensionality of the created vortices and their interaction are analyzed. Therefore Figure 9 displays a comparison of three span-wise y-position measurements at an angle of attack of $\alpha_{hl} = 0°$. Again, in all graphs the ordinates describe the measured flow-angle φ in the x-z plane and the abscissae the time course of the cycles. All black curves represent the ensemble averaged measurement signal and the grey lines their added / subtracted standard deviation. The origin of the x-z coordinate system (see Figure 1), referred to in the figure, is located at the mid-span nose-point of the high-lift airfoil at an angle of attack of $\alpha_{hl} = 0°$. The same z-positions are compared at y = 50 mm, y = 250 mm and y = 450 mm from mid-span.

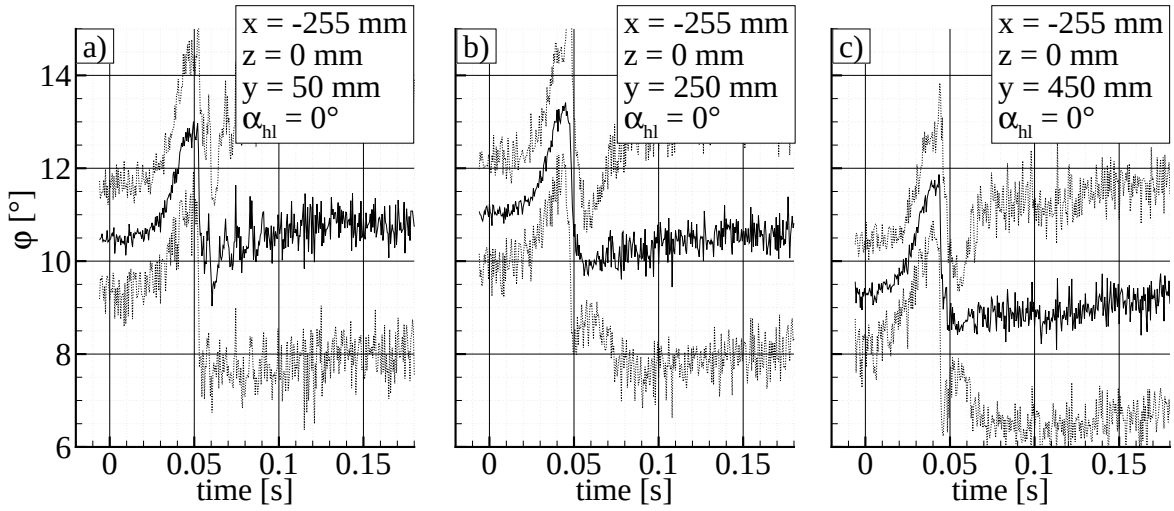

Figure 9: Span-wise ensemble averaged FHP measurements and their standard deviation ($\alpha_{hl} = 0°$)

As already indicated in the introduction the created vortices are quasi two-dimensional ([6]) as can be seen in the span-wise comparison. In all three measurement points the duration, the behavior and the induced absolute angles are almost identical as the vortices pass by the particular position. Once more, only the leading flank of the created vortices can be measured, whereas the trailing flank is damped. Real differences only occur in the streamline deviation caused by the high-lift airfoil circulation (mean angle φ). Towards the sidewall, at y = 450 mm, the measured mean angle φ decreases. This could be caused by the used sidewall droop-noses. With a local droop of 15° and an extension of 10% of the span ([4]), they influence the lift distribution and therefore the lower mean angle measured. In contrast to the non-drooped airfoil with a single suction peak (see Figure 5), the drooped airfoil features two smaller suction peaks at the nose and at its kink. This could decrease the deviation of the flow upstream of the wing. A second reason is purely geometrical. As the FHP was traversed at a constant z-position, the distance to the airfoils drooped surface increased near the sidewall. The FHP therefore measured effectively the less deviated flow further away from the surface. Further explanations for the decreasing mean angle can be found in the influence of the sidewall boundary layer, the interaction of the vortex generator with the sidewall boundary layer and the interaction of the high-lift airfoil with the sidewall boundary layer. It was not possible to quantify the influence of each effect on the basis of the acquired data.

A smaller mean angle φ and a damped trailing vortex flank can also be found in sidewall boundary layer measurements. Figure 10 shows ensemble averaged FHP measurements just at

the edge of the sidewall boundary layer. These measurements were conducted at z = 100 mm above the high-lift airfoil nose-point ($\alpha_{hl} = 0°$) and x = -425 mm in front of it. As this position is even further away from the airfoil surface, the above mentioned reasons for the smaller averaged angle φ apply as well. Figure 10 displays the whole phase of creating start/stop-vortices, to illustrate that only the leading flanks of the induced vortices are effective in the flow. Furthermore the measured φ angles of the induced vortices are smaller close to the sidewalls. A peculiarity of this measurement is the increased standard deviation for deflected vortex generator. At $\alpha_{vg} = 10°$ (during t = 0.06 to 0.26 s), the vortex generator wake and the interactions of the vortex generator with the sidewall boundary layer, apparently induce considerable fluctuations into the measured section.

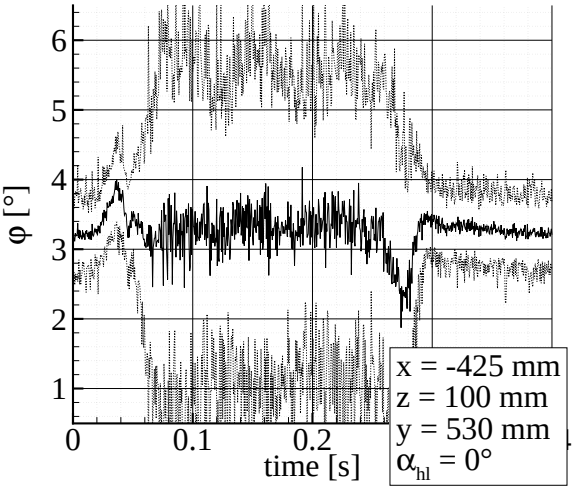

Figure 10: Ensemble averaged FHP measurements close to the sidewall boundary layer.

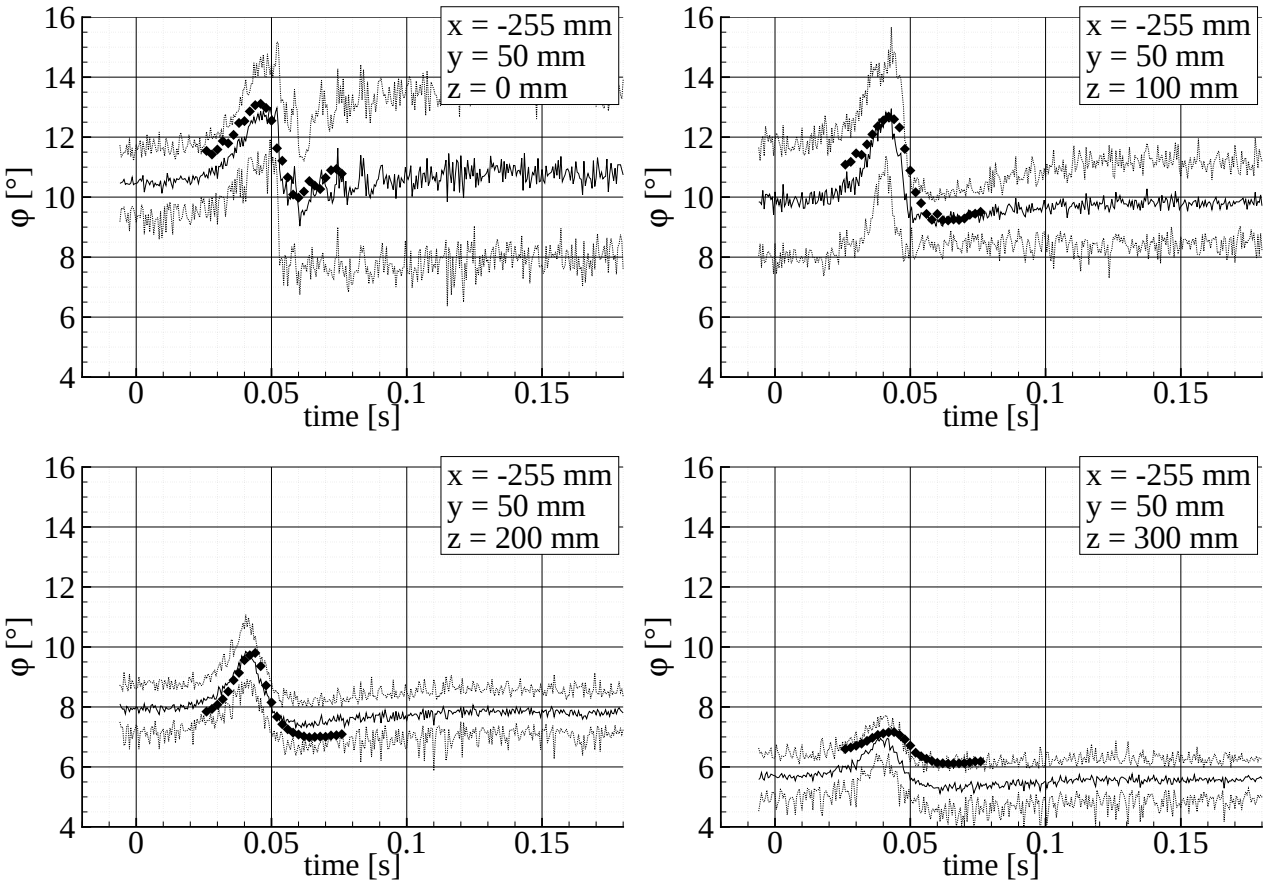

Figure 11: Comparison of ensemble averaged FHP measurements (-) and phased locked standard PIV measurements (♦) at $\alpha_{hl} = 0°$

To characterize the induced vortices in vertical extension and to confirm the accuracy of the utilised FHP measurement technique under dynamic conditions, Figure 11 shows a comparison between phased-locked standard PIV and FHP measurements at different z-positions in

mid-span at $\alpha_{hl} = 0°$. Again, displayed in lines are the FHP measurements and their standard deviations. The φ angles extracted out of phase-locked PIV measurements at the FHP measurement positions are marked with black diamond symbols. Each diamond symbol represents the result of a series of 300 double pictures. All series have been triggered by the movement of the actuator of the vortex generator drive (see Chapter 2). To scan the passing vortices, these phase locked measurements were repeated with a phase time shift of 2 ms. At all four z-positions the same flow characteristics were measured with both FHP and PIV. Here we observe a developed leading and a damped trailing flank of the induced vortices and a decreasing mean φ angle with increasing distance to the high-lift airfoil. Induced angle peaks, their duration and the deviation of the stream lines caused by the high-lift airfoil measured with PIV, are within the standard deviations of the FHP measurements. Speaking in total numbers, the two measurement techniques differ only by ± 0.5 ° in their results although no corrections concerning the unsteadiness of the measured flow, as proposed by [8] for example, have been applied during FHP measurements.

Completing the picture of the created vortices and their interactions with the high-lift airfoil at the leading edge, Figure 12 a) displays the pressure coefficient c_p over time of over 80 cycles ensemble averaged local static pressure measurements. A Kulite XCQ 93 sensor was positioned at ≈ 0.03 x/c and y = -50 mm off the midsection in the suction side of the leading edge of the high-lift airfoil. Figure 12 a) displays a comparison of the pressure signal at three different angles of attack, from top to bottom; $\alpha_{hl} = 6°, 4°, 0°$. Again, a distinct change in the signal can only be found for the leading flank of the vortices. Comparison with the PIV and FHP measurements (see Figure 11) shows good agreement of the time span of the disturbance. The beginning of the pressure signals rising edge should be shifted by 5.4 ms for comparison, as the distance between the Kulite and the measuring point of the FHP is $\Delta x = 273$ mm. Note that the induced pressure difference of $\Delta c_p = 0.42$ is independent of the angle of attack of the high-lift airfoil.

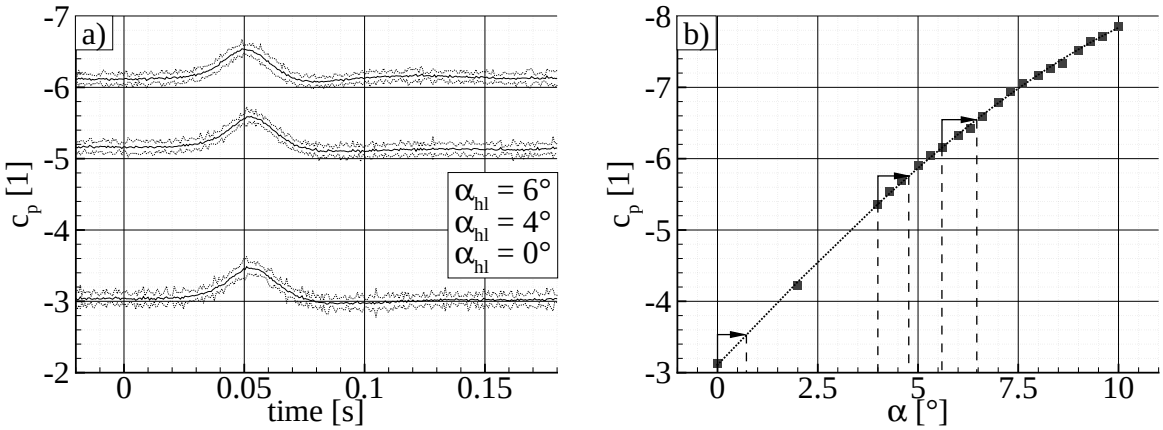

Figure 12: a) Ensemble averaged static pressure measurements and standard deviations at the high-lift airfoil leading edge (0.03 x/c) at $\alpha_{hl} = 6°, 4°, 0°$ b) mean static pressure for $\alpha_{hl} = 0°$ to 10° at 0.03 x/c

Figure 12b) shows in squares the time averaged static pressure coefficient c_p of a pressure tap (compare Figure 5) next to the Kulite position at ≈ 0.03 x/c. Arrows and dashed lines mark the change in angle of attack needed to cause a pressure difference of $\Delta c_p = 0.42$. The changes range from $\alpha_{hl} = 0.75°$ to 0.9° for $\alpha_{hl} = 0°, 4°, 6°$. This is less than the angle of $\varphi \approx 2°$ which the vortices induce at a position 255 mm upstream the high-lift airfoil. This supports the presumption that the induced vortices change their impact, as they travel over the airfoil.

3.2.2 Disturbances at the trailing edge

A major challenge for the chosen points of investigation is the fact, that the trailing edge pressure is not very sensitive to changes in angle of attack (see Figure 5).

Figure 13 shows a comparison of time resolved static pressure measurements at $\alpha_{hl} = 4°, 6°$. In this graph the measurement position is at the suction peak of the flap at x/c = 0.91. Displayed is every 32^{nd} sample of a 50 kHz sampling series, which has been ensemble averaged over 80 cycles. Taking into account the sensor position at the airfoil suction side and a first estimation of the disturbances convection velocity of 50 m/s the pass-by of the start-vortex should occur at the time t ≈ 0.06 s. However, for the displayed angles of attack, flow changes seem to become effective not before time t = 0.07 s. Moreover, not only that the signal occurs later than expected, also the size of the disturbances seem to have grown from a signal of $\Delta t \approx 40$ ms at the main element leading edge (see Figure 12), to one of $\Delta t \approx 60$ ms.

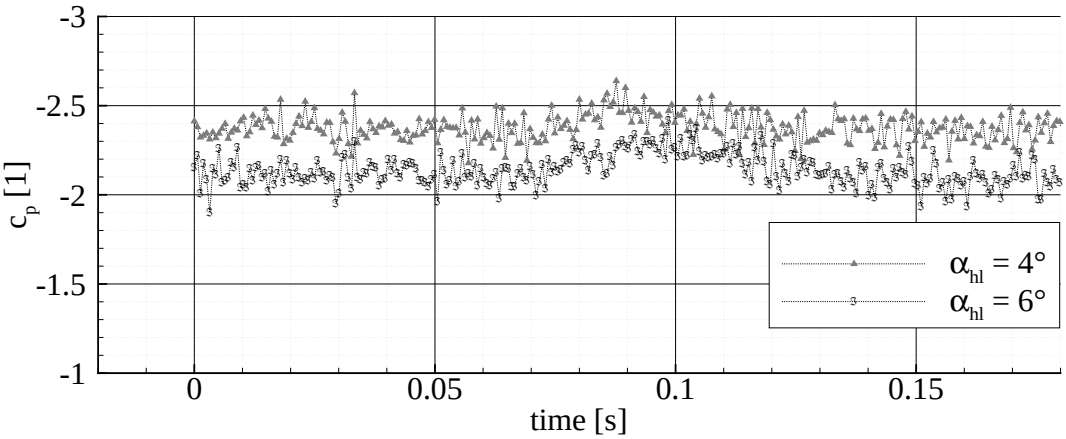

Figure 13: Comparison of ensemble averaged time resolved static pressure measurements at $\alpha_{hl} = 4°, 6°$

To find reasons for this behavior, it is helpful to investigate the flow topology in different heights. Figure 14 shows a comparison of ensemble averaged FHP and phase locked standard PIV measurements. Again the black lines represent the FHP measurements and the grey lines describe their standard deviations. Each diamond symbol stands for the angle information of the measuring point described in x, y, z-coordinates extracted from PIV measurements. PIV measurements with steady un-/deflected vortex generator are added with triangle symbols at times t = 0.03 s and t = 0.13 s. Origin of the used coordinate system is the center of the main element leading edge at $\alpha_{hl} = 0°$. Hence the first measurement (z = 35 mm) has been conducted at x = 1.01 x/c and around 65 mm above the flap. The time interval between each phase locked PIV measurement is 2 ms. Important is the highly dynamical flow condition at the trailing edge of the high-lift airfoil provided by interactions between a partly detached flap, the gap flow and a turbulent boundary layer of the main element. Using the steadily calibrated FHP in such a dynamic flow, a large variance occurs in the measurements. Therefore the steady PIV measurements (▲) with steady un-/deflected vortex generator are used in the intervals between the pitches of the vortex generator, to indicate systematic measurement errors of the FHP measurements. Nevertheless, both measuring methods reproduce not only similar trends, but same characteristics. Note worth in these measurements is a negative induced angle. This is an indication for the trailing flank of the vortex, whereas in the leading edge region of the flap the airfoil reacts as if only a positive induced angle (Figure 13) would be present. As the measurement position moves away from the airfoil, both flanks of the vortex re-emerge in the measurements (see Figure 14 z = 185 mm). Here, compared to a position upstream of

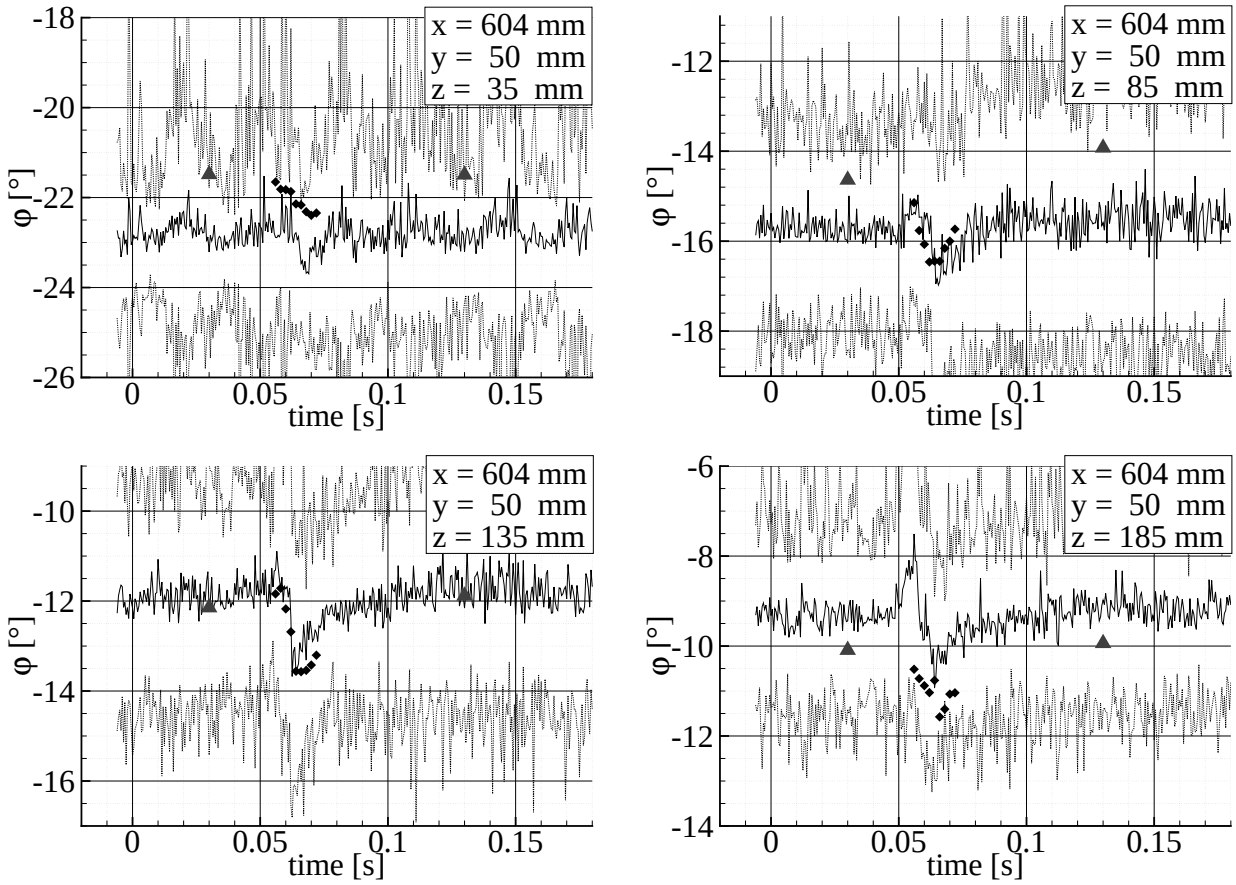

Figure 14: Comparison of ensemble averaged FHP (-) and phase locked PIV (♦▲) measurements above the flap at $\alpha_{hl} = 0°$

the high-lift airfoil (see Figure 7), the maximum induced φ angle has not changed significantly with a value of $\varphi \simeq 2°$. In both cases the measurement position is located away from the airfoil surface, whereas at the leading edge of the high-lift airfoil the dynamic effect of the vortex corresponds to a static change in angle of attack of $\alpha_{hl} \approx 1°$ (see Figure 12). Apparently, the induced disturbances are damped the stronger the closer they are to the surface.

4 Conclusion

A two element high-lift airfoil was investigated experimentally in disturbed flow. As disturbances quasi two-dimensional vortices have been created in a closed test-section upstream of the airfoil. Several measurement techniques, like Particle Image Velocimetry (PIV), time resolved static pressure measurements, measurements of the static pressure distribution of the high-lift airfoil, oil flow visualization and Five Hole Probe (FHP) measurements were utilized to investigate the characteristics of the vortex-airfoil interactions. All time resolving measurements were performed at two areas of interest: One is located close to the leading edge of the main element, which is the upstream area, and one is located at the trailing edge of the main element including the flap, which is the downstream area.

As a starting point time averaged flow states served to judge the overall flow and the airfoil behavior. In a second step the signature of the created vortices was investigated in the interference region with the airfoil. Also the influence of the angle of attack α_{hl} of the

airfoil was documented as well as the span-wise characteristic of the vortex interaction. By comparing different measurement techniques the accuracy of the results were investigated. An outcome of the measurements is, that the interaction of the created vortex with the leading edge region takes about 40 ms which is similar to measurements in the otherwise empty test-section [5]. Also the amplitudes of the induced angles are comparable at corresponding positions. Whereas in otherwise empty test-section every vortex induces positive and negative angles, as the high-lift profile is present, only the leading flank of the vortex appears and interacts at the leading edge. The measurements prove the quasi two-dimensional character of the created vortices ([6]). As a third step, measurements have been conducted at the main element trailing edge/flap position. Here the induced disturbances appear to interact for about 60 ms with the profile. Moreover, negative induced angles were measured with the FHP. This is an indication for the trailing flank of the vortex, whereas the static pressure measurements on the flap and the leading edge measurements deliver exclusively positive induced angles. We find that the induced flow disturbances become smaller near the airfoils surface.

For future experiments additional standard PIV measurements in span-wise planes on the flap suction side are planned. With these investigations the propagation of the quasi two dimensional disturbances over the airfoil shall be regarded. Hot-film measurements are planned to supplement the gathered database by shear stress measurements at the trailing edge of the main element and on the flap. Additional time-resolved static pressure measurements in the flap bay are planned to get a view of the gap flow dynamic. For a view on the high-lift airfoil wake dynamic hot-wire measurements are planned.

Acknowledgments

The members of the FOR 1066 research group gratefully acknowledge the support of the "Deutsche Forschungsgemeinschaft DFG" (German Research Foundation) which funded this research.

References

[1] Barlow J.B., Rae W.H., Pope A.: "Low-Speed Wind Tunnel Testing" Wiley-Interscience Publication 1999

[2] Broeren A. P., Bragg M. B.: "Spanwise Variation in the Unsteady Stalling Flowfields of Two-Dimensional Airfoil Models" AIAA Journal, September 2001, Vol. 39, No. 9 : pp. 1641-1651

[3] Freymann R.: "Die Böensimulationsanlage des 3m x 3m Niedergeschwindigkeitskanals der DFVLR in Göttingen", DFVLR-FB 85-04 1985

[4] Hahn D., Scholz P., Radespiel R. "Experimental evaluation of the stall characteristics of a two-element high-lift airfoil" Second Symposium "Simulation of Wing and Nacelle Stall", Braunschweig, 2010, https://www.for1066.tu-bs.de/attachments/5-Hahn.pdf

[5] Hahn D., Scholz P., Semaan, R., Radespiel R., Müller-Eigner R. "Erzeugung definierter Querwirbel in einer geschlossenen Messstrecke" 60. Deutscher Luft- und Raumfahrtkongress 27. - 29. September 2011, Congress Zentrum Bremen.

[6] Hahn D., Scholz P., Radespiel R. "Vortex generation in a low speed wind tunnel and vortex interactions with a high-lift airfoil" AIAA-2012-3024, 30th AIAA Applied Aerodynamics Conference, New Orleans, Louisiana, June 25-28, 2012.

[7] Helmke C., Auerswald T., Raasch S., Bange J.: "Comparison of two methods to provide highly resolved atmospheric turbulence data for simulations of wing and nacelle circulations" Second Symposium "Simulation of Wing and Nacelle Stall", Braunschweig, 2010, https://www.for1066.tu-bs.de/attachments/12-Helmke.pdf

[8] Johanson E. S., Rediniotis O. C. "Unsteady Calibration of Fast-Response Pressure Probes", Part 1,...,3, AIAA-Journal, Vol 43, No. 4, April 2005.

[9] Kähler CJ, Sammler B, Kompenhans J: "Generation and control of particle size distributions for optical velocity measurement techniques in fluid mechanics." Exp. Fluids 33, pp. 736-742, 2002

[10] Krag B.: "Vermessung des Böenfeldes hinter harmonisch schwingenden Böenerzeugern im Modell-Unterschall-Kanal (MUK)" 1982. Forschungsbericht. Deutsche Forschungs- und Versuchanstalt für Luft- und Raumfahrt ; 82-26

[11] Lee T., Gerontakos P.: "Investigation of flow over an oscillating airfoil", Journal of Fluid Mechanics 2004, Vol. 512, pp. 313-341

[12] Schlichting H., Truckenbrodt E.: "Aerodynamik des Flugzeuges" Springer Verlag Band 1, 2 1962

[13] Semaan R., Scholz P. " Pressure correction schemes and the use of the Wiener deconvolution method in pneumatic systems with short tubes" Experiments in Fluids: Volume 53, Issue 3 (2012), Page 829-837

[14] Swalwell K. E., Sheridan J., Melbourne W. H.: "The Effect of Turbulence Intensity on Stall of the NACA 0021 Airfoil", 14th Australasian Fluid Mechanics Conference Adilaide Australia 10-14 December 2001

[15] Wild J.: "Experimental investigation of Mach- and Reynolds-number dependencies of the stall behaviour of 2-element and 3-element high-lift wing sections", 50th AIAA-Aerospace Science Meeting 9-12 Jan 2012 Nashville, Tennessee.